From waste to resources: transforming olive leaves to hard carbon as sustainable and versatile electrode material for Li/Na-ion batteries and supercapacitors

From waste to resources: Transforming olive leaves to hard carbon as sustainable and versatile electrode material for Li/Na-ion batteries and supercapacitors.

Hamideh Darjazi[a*], Luca Bottoni[a], Hamid Reza Moazami[b], Seyed Javad Rezvani[c], Leonardo Balducci[a], Leonardo Sbrascini[a], Antunes Staffolani[a], Alessia Tombesi[d], Francesco Nobili[a,e]

[a]*School of Science and Technology, Chemistry Division, University of Camerino, Via Madonna delle Carceri - ChIP, Camerino (MC) 62032, Italy.*

[b]*Faculty of Chemistry, Shahid Beheshti University, G. C., 1983963113, Evin, Tehran, Iran.*

[c]*School of Science and Technology, Physics Division, University of Camerino, Via Madonna delle Carceri 9B, Camerino MC 62032, Italy.*

[d]*School of Pharmacy, Chemistry Division, University of Camerino, Via Madonna delle Carceri - ChIP, Camerino (MC) 62032, Italy.*

[e]*GISEL—Centro di Riferimento Nazionale per i Sistemi di Accumulo Elettrochimico di Energia, INSTM, via G. Giusti 9, 50121 Firenze, Italy.*

** Correspondence: hamideh.darjazi@unicam.it*

Highlights

- Hard carbon (HC) material was synthesized as an electrode for energy storage application.
- The HC electrodes exhibited high capacities and promising cycling performances for Li/Na-ion batteries.
- The diffusion behaviour of electrodes is discussed for both for Li/Na-ion batteries.
- The electrodes also delivered high performance upon long cycling for supercapacitors.

Abstract

Over the last few years, biomass-derived hard carbon materials are drawing more and more attention because of their high abundance, cost breakdown, high performance, and fast regeneration. In this context, the synthesis of hard carbon from olive leaves, a widely available by-product of table olive and olive oil industries, is here reported and its performance, as a sustainable electrode material for Li-ion batteries (LIBs), Na-ion batteries (NIBs), and supercapacitors (SCs), are evaluated. According to the information acquired by structural characterization, a disordered structure is confirmed for the synthesized hard carbon. When

tested as anode for LIBs and NIBs, electrodes based on Na-CMC green binder show discharge capacities of 331.0 mAh g^{-1} and 265.4 mAh g^{-1} at 1C, respectively, with promising cycling stability. In SC application, the electrode delivers a high specific capacitance of 169.6 F g^{-1} at 0.5 A g^{-1} and remarkable capacity retention of 96.7% after more than 20000 cycles at 10 A g^{-1}. As a result, this work confirms the possibility to use olive leaves-derived hard carbon material for the low-cost, environmental-friendly fabrication of electrodes with high energy and power capabilities.

Keywords: Biowaste-derived hard carbon; Li-ion batteries; Na-ion batteries; Supercapacitors.

<Graphical abstract>

1. Introduction

How to respond to the needs of billions of people worldwide with the beat of climate change? To mitigate the most major and intricate challenges facing humanity today, we must learn to re-think the economic system we are experiencing every day and act upon it.

In many application areas, some of the most practical technologies for storing energy are Li-ion batteries (LIBs), Na-ion batteries (NIBs), and supercapacitors (SCs) [1]. The earliest attention to LIBs and NIBs has drawn in the 1980s [2]. Heretofore, LIBs have become the most advanced energy storage devices penetrated into everyday life [3], while the development of NIBs was sluggish [2]. The utilization of LIBs has extensively extended from small and light battery packages in portable electronics (laptops, cell phones, etc.) to large-scale applications in electrified vehicles (hybrid, plug-in hybrid, and fully electric), thanks to their high energy and power densities [2,4–6]. However, there are concerns associated with the limitation of Li resources to meet the worldwide demands and increase the price of lithium carbonate [7]. Thus, in order to meet the needs for future energy storage applications, NIBs have attracted considerable attention as potential LIBs substitutes [8,9] owing to similar chemical properties of Na with Li in many facets, more than 1000 times higher earth's abundance of Na resources

than those of Li, and lower cost [2]. Concerning SCs, they are used for a huge number of applications as the foremost energy storage devices with outstanding properties including a high power density, a reasonable energy density, and a long cycle life [10]. In order to develop these practical technologies (LIBs, NIBs, SCs) in terms of electrochemical performance, cost, safety, and sustainability, the most viable approach is the use of cost-effective, environmentally benign, and abundant materials. For commercial alkali-ion batteries and SCs, carbonaceous materials are considered as prospective electrode materials due to their low cost, high abundance, and specific structural and electronic properties [1,11].

On the other hand, products have been designed up to now in a linear model from the cradle to the grave, from production to consumption to waste. The market is beginning to realize that it can make value by reusing and recycling products in a closed loop, whereby they do not become waste but vital resources again [12]. A disruptive transformation in the industry is pinned to a change in the consumer market and its demands for sustainable goods. The production surplus can and should be transformed into secondary raw materials, from the perspective of the circular economy.

With the aim of reusing and disposing of waste materials and increasing the sustainability of energy storage devices, an extensive research effort has been devoted to the production of hard carbons (HCs) from raw and waste biomasses [13]. For instance, corn cobs [14], banana [15], apple peel [16], phenolic resin [17], citrus peel [18], peat moss [19], rice husk [20], tire [21], rose [22], peanut shell [23], pitch and lignin [24], leaf [25], and cotton [7] have been reported as secondary raw materials for the synthesis of HCs as anode materials for NIBs. Due to the similarity of the Na^+ intercalation mechanism to Li^+ [3], some works have also been reported comparing the performances in NIBs and LIBs, of anodes based on HCs prepared by using waste biomasses, such as orange peel [26], olive pits [27], peanut shell [23], etc. In addition, the fast kinetics of charge storage at HCs surface, due to the high surface areas, makes them

also feasible for application in SCs [22,28,29]. SCs of this type known as electrostatic or electric double-layer capacitors (EDLCs) are able to store charge at their surface by creating electrostatic charge diffusion and adsorption in a Helmholtz double layer at the electrode/electrolyte interface [22].

It should be noted that the main aim of the paper is to demonstrate the feasibility of a sustainable synthesis, from food-waste raw material, of a carbon, which is suitable for three kinds of applications in energy storage such as LIBs, NIBs, and EDLCs (see Fig. 1). Sustainable hard carbon obtained by chemical acid activation and pyrolysis of olive leaves and the enhanced electrochemical performances indicate that this low-cost and eco-friendly material, could be a promising candidate for Li/Na-ion batteries and supercapacitors. In fact, the leaf consists of cellulose, hemicellulose, and lignin [30], offering a good template for the preparation of carbon with high porosity through acid and heat treatment [31]. Further, leaves with anisotropic surfaces (back surface is porous but upper surface is non-porous) not only can facilitate pathways for electrolyte by providing extra channels but also provide high adhesion strength of the electrode film to the substrate as the electrode for batteries and supercapacitors [25]. The choice of olive leaves is because of a widely available by-product of table olive and olive oil industries. In many countries, people worldwide use daily olive oil in their cuisine. To date, the products of the olive tree are also used for cosmetics, medicine, etc. Olives are harvested most commonly by machine or handheld tools, in which the branches are shaken, making the olives and leaves drop. Leaves are then left on the ground, resulting in easier to collect than roots, trunks, or pits. Besides, the interest in olive leaves as waste biomass comes from the fact that Italy is well-known for the second-largest amount of olive oil production. Italy produces an average olive oil quantity of around 550,000 tons over the last four years. Thus, olive farming in Italy makes huge quantities of olive leaf waste which can be considered as a waste

biomass raw material characterized at the same time by wide abundance and ease of collection and should be managed from an environmental point of view.

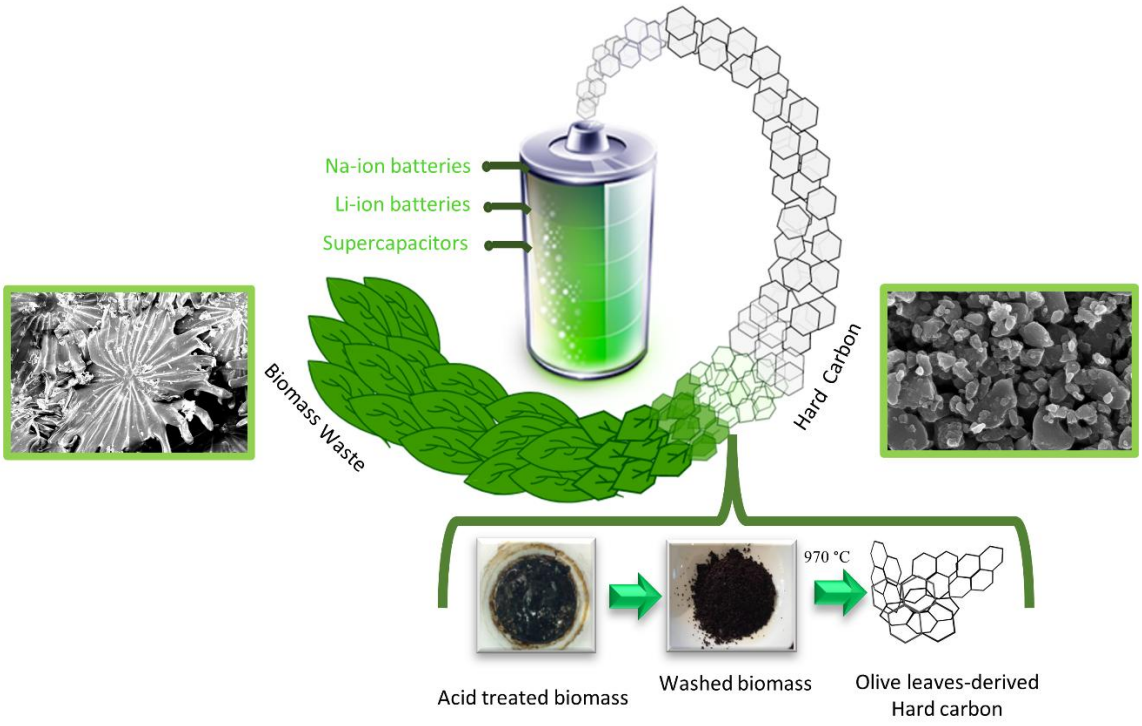

Fig. 1. Sustainable utilization of biomass waste for the synthesis of hard carbon for 3 applications; LIBs, NIBs, and SCs.

2. Experimental

2.1 Material synthesis

The olive leaves are directly collected from the Marche region, Italy. The olive leaves were washed with distilled water and dried at 80 °C for 3 days in an oven. The raw material was smashed and immersed in the solution of dilute hydrochloric acid (HCl) for three days to obtain a more porous structure and to remove any residual impurities (leaves and HCl with a weight ratio of 1:3). Afterward, the product was washed using ultrapure water several times until pH=7 was obtained and then stored at 80 °C overnight. Olive leaves-Derived Hard Carbon, hereafter designated as OLDHC, was prepared by the pyrolysis of the product in a tubular furnace at 970 °C for 6 h under argon atmosphere after a heating ramp of 5 °C min^{-1} [12] (the pyrolysis yield

was ~ 24%). The mentioned temperature was used because small molecules, such as H_2O, CO_2, and N_2 among others, are released, resulting in high porosity materials, and low particle density for a heat treatment temperature near 1000°C [11]. At higher temperatures (>1200 °C) the nature of the pores could be less open, leading to decreased BET (Brunauer, Emmett and Teller) surface areas [11] and resulting in lower performance in energy storage devices. Besides, specific surface area and pore-size distribution are the two most essential aspects influencing the performance of carbonaceous materials in EDLCs [1], therefore, HCs prepared for this purpose were heated near 1000°C [22,28,29]. Ultimately, the resultant powder was milled in a Retsch S100 ball mill with a speed of 400 rpm for 4 hours (agate jar of 50 mL and agate ball diameter 10 mm, ball-to-powder ratio= 4:1 in weight).

2.2 Material characterization

The structure of the OLDHC powder was characterized by X-ray diffraction (XRD) (Bragg–Brentano geometry, Cu-Kα, λ = 1.54059Å) and Raman spectra (Horiba IHR 320, wavelength 532 nm). From XRD, the interlayer spacing (d_{002}), the stacking height (L_c), and the graphene stacking layers number (n) were defined. The d_{002} was calculated based on Bragg's law: $d_{002} = \lambda / 2\sin(\theta_{002})$, with λ = 0.154 nm, while the L_c was obtained from Scherrer's equation: $L_c = 0.9\lambda / \beta_{002}\cos(\theta_{002})$, where β_{002} is equal to the full width at half maximum (FWHM) of 002 peak. n was obtained by dividing L_c by d_{002} [12,32]. By Raman spectra, the graphitic domain size (L_a) was revealed from $L_a = (2.4 * 10^{-10})\,\lambda^4 (I_D/I_G)^{-1}$, with λ = 532 nm [19,32]. The Fityk software was used to perform background removal and normalization. The deconvolution of the spectra was carried out by using Lorent-zian-Gaussian fitting on Spec5 software. The morphology of the samples and the distribution of elements were explored by scanning electron microscopy (SEM) analysis using a FE-SEM Cambridge Stereoscan 360 electron microscope coupled with energy dispersive X-ray spectroscopy (EDX). The Infra-Red spectra of the pristine olive leaves were carried out using a Perkin-Elmer Spectrum Two FTIR spectrometer

within the wave number range of 500 to 4000 cm^{-1}. To study pore characteristics, nitrogen adsorption-desorption isotherm was performed at −195.8 °C in a Micrometritics ASAP 2020 analyzer on a sample preliminarily outgassed for 12 h at 200 °C. The specific surface area values were calculated by the linear plot in the relative pressure range.

X-ray Photoemission Spectroscopy (XPS) measurements were done using an in-house XPS apparatus. The powder was shaped into pellets and was introduced through a specially designed load lock chamber into the measurement chamber. For measurement, a focused Al K_α radiation (hv= 1486.6 eV) with the base chamber pressure of 10^{-9} mbar was utilized. To confirm the homogeneity of the sample as well as radiation degradation prevention, different points on the sample were examined with a short dwell time. Core peaks were evaluated via a non-linear Shirley background.

2.3 Electrode preparation and electrochemical tests for LIBs and NIBs

The working electrode was prepared by mixing the OLDHC active material with conductive carbon SuperC-65 and Na-carboxymethyl cellulose (CMC) (Sigma-Aldrich) binder (80:10:10 in weight) in deionized water, then coating the acquired slurry onto Cu foil for LIBs and onto Al foil for NIBs by using a doctor blade. After drying the laminates at room temperature overnight, the anode electrodes were cut and punched and then vacuum dried in BUCHI Glass Oven Drying at 120 °C for 10 hours. The main purpose of vacuum-drying is to allow the removal of moisture under vacuum. OLDHC-based electrodes were evaluated in half cells using either metallic Li or Na, correspondingly, both as the counter and reference electrode in T-shape polypropylene Swagelok-type 3 cells. Assembly was performed in an argon-filled glove box (Jacomex GP-campus, oxygen, and moisture content less than 0.8 ppm). 1 M $LiPF_6$ in a mixture of 1:1 (v/v) ethylene carbonate (EC)/dimethyl carbonate (DMC) (preformulated by Solvionic, France) electrolyte was used for LIBs, while 1 M $NaClO_4$ (Sigma-Aldrich) in EC: PC (Sigma-Aldrich) electrolyte was used for NIBs. For both LIBs and NIBs, a glass fiber

disk (Whatman GF/A) was utilized as separator. The electrochemical behavior of the electrodes was characterized by a VMP-3 multichannel electrochemical workstation (Bio-Logic, France). All the cells were kept 12 h at open circuit voltage (OCV) before running the measurements. Cyclic voltammetry (CV) was obtained in the potential range within 0.01–3.00 V at 0.05 mV s^{-1} scan rate. All potential values are given *vs.* Li^+/Li and Na^+/Na redox couples for LIBs and NIBs, respectively. GCPL tests of the electrodes were collected in the same potential range at 1C= 300 mA g^{-1} with respect to active material mass. In addition, the C-rate capability of the electrode was tested in the C/10 to 2C range (5 cycles at every rate), and capacity recovery was subsequently evaluated at C/10 for LIBs and NIBs. Electrochemical impedance spectroscopy (EIS) measurements were carried out at each 10^{th} cycle at E = 0.5 V bias potential, with an AC amplitude of 10 mV, in the frequency range 10 mHz < f < 100 kHz. The GITT measurements were carried out at C/10 with pulse time τ= 0.5 h and relaxation period of 2 h.

2.4 Electrode preparation and electrochemical test for EDLCs

To make a slurry, the same procedure has been applied for EDLC electrodes, by using Polyvinylidene fluoride (PVDF) binder dissolved in a N-methyl pyrrolidone (NMP) (both chemicals from Sigma-Aldrich) slurry. The mixed slurry was uniformly coated onto a nickel foam current collector and heated at 70 °C for 2 h and then dried at room temperature. After drying, the electrode was pressed using a rolling press. The electrochemical behavior of the OLDHC electrode was tested via a standard three-electrode system in 6.0 M KOH aqueous solution using a SP-240 electrochemical workstation (Bio-Logic, France). A Pt foil and an Ag/AgCl electrode served as the counter and reference electrodes, respectively. The cyclic voltammetry (CV) was tested between -1.2 V to 0 V *vs.* SCE at the scan rates of 2, 5, 10, 25, 50, 75, 100 mV s^{-1}. The charge/discharge behavior was evaluated at different current densities between -1.2 V to 0 V *vs.* SCE, while the cycling behavior of the electrode was estimated at 10

A g^{-1} up to more than 20000 cycles. EIS measurements were carried out in the frequency range from 10 mHz to 100 kHz, with an AC amplitude of 10 mV over OCV.

3. Results and discussion

3.1 Structural analysis

Chemical, structural, and morphological investigation of pristine olive leaves was performed. SEM (Fig. S1a-c) reveals a typical morphology of olive leaf in which the surface has scale-like, peltate trichomes that often overlap. The distribution of elements was examined by EDX analysis, shown in Fig. S1d. The result shows the presence of carbon, oxygen, calcium, potassium, silicon, aluminum, and magnesium in pristine olive leaves. FTIR analysis shows the presence of nitrogen in the pristine olive leaves (Fig. S2a). The elemental analysis also shows the small amounts of nitrogen in both pristine olive leaves and olive leaves-derived hard carbon, which can be expected to increase the conductivity of the sample (Fig. S2b,c). The structure of OLDHC has been evaluated by X-ray diffraction (XRD) and Raman spectroscopy, as shown in Fig. 2a-d. The XRD pattern of the ball-milled sample (Fig. 2a) is typical of HCs (amorphous structure with a lack of long-range order) and shows two broad peaks located around $2\theta = 23^{\circ}$ and $2\theta = 44^{\circ}$, which are related to the (002) and (100) planes of graphite, respectively. The calculated interlayer spacing (d_{002}) of OLDHC powder, which is around 0.38 nm, represents a random combination of graphitic and turbostratic stacking [33]. This value is higher than that of graphite ($d_{002} = 0.33$ nm) and of soft carbon ($0.34 \leq d_{002} \leq 0.36$ nm), which simplifies Na^{+} ion diffusion between carbon layers [34]. The stacking height (L_c) value is about 0.75 nm, which is in good line with the reported sp^2 carbonaceous materials. In addition, the average graphene stacking layers number (n) was determined around 1.98. To investigate the OLDHC structure before and after ball milling, Raman spectroscopy has been utilized. The spectrum of both samples show D-band peaks at ~1348.39 cm^{-1}, G-band at ~1582.94 cm^{-1}, and two broad peaks at about 2600 cm^{-1} and 2887 cm^{-1}, corresponding to 2D and D+G bands, which

are typical for all graphitic materials (Fig. 2b) [17]. The D-band (the defect-induced band) is associated with vacancies and a disordered state of carbon, while the G-band (the crystalline graphite band) corresponds to the C-C stretching bond in the graphitic carbon phase, caused by the sp^2-hybridized atom vibration mode in the carbonaceous materials [35]. Fig 2c,d show the fitted results of the OLDHC before and after ball milling. As can be observed, D* peak can be assigned to the sp2-sp3 bonds, D** peak is correlated to the vibrational response of the amorphous carbon content such as adsorbed molecules, molecular fragments, or functional groups, and D' band is another lattice vibration of the surface graphene layers [36]. The intensity ratio of D-bands over G-bands (I_D/I_G), which reveals the disorder of the prepared hard carbon, is found to be 1.10 and 1.16 for powder before and after ball milling, respectively, representing that the degree of defect increased by ball milling [37]. Besides, the 2D band provides information about the graphitization degree, while the D+G band is associated with the defect activated process for elastic scattering [17]. The graphitic domain size (L_a) was calculated at around 17.47 and 16.57 nm for powder before and after ball milling. Therefore, the calculated crystallographic parameters by XRD and Raman spectra, confirm a certain degree of graphitization, together with a disordered structure of OLDHC material [17,32].

To evaluate the surface chemistry of the HC before and after ball milling and the existence of various surface terminal groups, XPS of the powders was carried out. Fig. 2e shows the XPS spectra of both powders, while Fig. 2f, g shows the fitted spectra of C 1s and relative C-containing chemical species for both samples. The spectra of both samples are very similar and reveal the presence of heteroatoms of O and N on the surface of both samples. The existence of oxygen is due to partial oxidation of the surface during synthesis, which slightly increased after ball milling. It is well known that the graphenic sheets in HC can contain defects, edges, functional groups, and heteroatoms [11]. The heteroatoms act as electron donors toward the graphenic sheets and increase the electron density at defects in the graphenic layer, leading to

complex reduction reactions on the surface [11]. Therefore, they can provide additional sites for the reversible adsorption of Li^+/Na^+, improving the electronic conductivity and electrochemical reactivity [23].

The nitrogen adsorption-desorption isotherms can be observed for the material before and after ball milling (Fig 2h,i), which are the typical IV isotherms with a distinct hysteresis loop at a relative pressure P/Po between 0.4 and 1, representing the presence of micropores and mesopores [22]. To be specific, the Brunauer-Emmett-Teller (BET) surface area, pore diameter according to density functional theory (DFT), and BJH (Barrett, Joyner, and Halenda) desorption average pore diameter before ball milling were determined to be 681.64 m^2/g, < 0.39 nm, and 6.02 nm, respectively (Fig 2h). However, these values were improved to 839.33 m^2/g, < 0.49 nm, and 4.02 nm after ball milling (Fig 2i). As shown in the inserts of Fig. 2h,i the sample after ball milling shows micropores mainly located at 4 nm, revealing that the ball milling process allowed the biochar to be well-defined porous fragments with more uniform diameters. The enhanced BET area and pore size distribution of ball-milled powder allow more electrolyte to enter the pores, enhancing the charge storage ability [24].

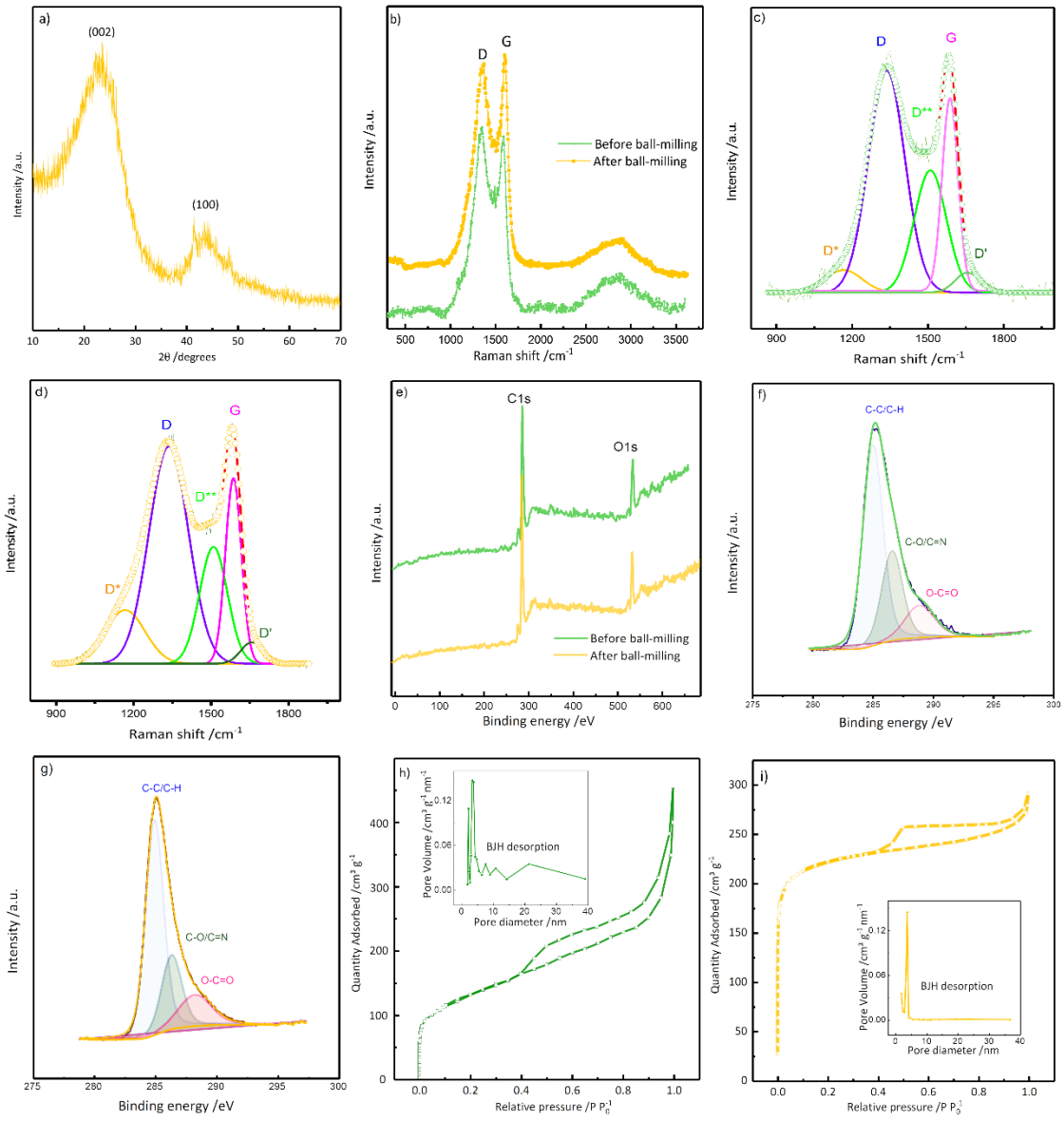

Fig. 2. Chemical and physical characterization of OLDHC powder: (a) XRD pattern; (b) Raman spectra; (c) De-convoluted Raman spectra before ball milling and (d) after ball milling Raman; (e) XPS spectra; (f) C 1s core-level before ball milling and (g) after ball milling; (h) Nitrogen adsorption-desorption isotherm and pore size distribution (insert) before ball milling and (i) after ball milling.

The SEM morphologies of the prepared hard carbon are shown in Fig. 3 a, b, before and after ball milling. Both present block morphology and fine fragments [32]. However, after ball-milling an obvious decrease in the size of particles and less agglomeration can be detected in the OLDHC powder. Minimizing particle size and inhibiting particles from aggregating can have a considerable impact on the surface storage mechanisms, by improving specific surfaces,

increasing conduction, enlarging active sites, and finally providing extra capacity [12]. The elemental composition assessed by EDX analysis reveals that apart from carbon and oxygen, there is a small quantity of Cl impurities which is originated from acid treatment (Fig. S3).

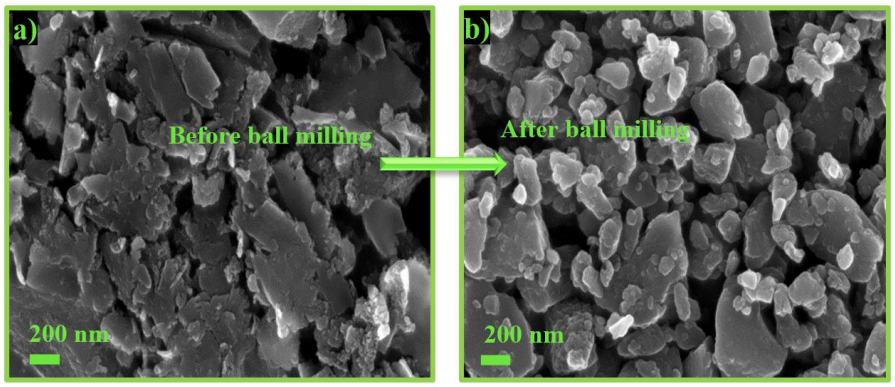

Fig. 3. (a) SEM images before ball-milling, and (b) after ball-milling.

3.2 Lithium storage performance

The lithium and sodium storage in hard carbon materials still remains with a content of discussion due to the complexity of the hard carbon microstructure, which includes heteroatoms, defect and edge sites, lateral size and thickness of graphitic layers and micropores [38]. For instance, Steven et al. evaluated the storage mechanism of the carbonaceous material with in-situ scattering study [39,40]. They revealed the model of "intercalation-adsorption", meaning that intercalation of alkaline ions into pseudo-graphitic regions at higher potential (sloping potential curve), and adsorption of ions in micropores created by the pseudo-graphitic domains, leading to a plateau at low potential [39,40]. On the contrary, more recent investigations proposed the mechanism of "adsorption-intercalation". This suggests that the high-potential sloping curve is related to alkali ions adsorption in the defect and edge sites, while low-potential plateau is associated to intercalation between parallel graphene sheets [41]. The lithium storage performance of the ball milled OLDHC electrode has been characterized by cyclic voltammetry (CV) and galvanostatic discharge/charge cyclation in the potential window of 0.01-3.00 V in half cells *vs*. Li^+ /Li. The CV profiles obtained during the first four

cycles at a scan rate of 0.05 mV s^{-1} are shown in Fig.4 (a). During the first cathodic scan process, a large irreversible capacity, evidenced by overlapped features in the region between 1 and 0.5 V, is ascribed to the irreversible reactions of electrolyte with surface functional groups and solid electrolyte interphase (SEI) formation [42]. Upon the subsequent anodic and cathodic scans, two reversible and sharp oxidation/reduction peaks located at around 0.1 V are visible, together with two broad shoulders in the 0.1 to 1.5 V. According to "adsorption-intercalation" mechanism, the sharp peaks are due to Li^+ ion intercalation/deintercalation, while the broader features can be assigned to surface adsorption/desorption phenomena. The E vs. Q profiles and cycling performance at 1C rate are shown in Fig.4 (b, c). The E vs. Q profiles is typical of HCs, consisting of two steps, a potential sloping region extending to around 0.1 V, and a low potential plateau, which describe the same adsorption-intercalation features evidenced in CV. The electrode exhibits an irreversible specific capacity of 643.7 mAh g^{-1} and Coulombic efficiency of around 48% upon the first cycle, performed at 1C. As mentioned before, in the initial cycle, the irreversible capacity is principally because of the irreversible SEI film formation, the irreversible reaction between Li and surface functional groups, and other side reactions [43]. Nevertheless, the Coulombic efficiency quickly approaches 99% after few charge/discharge cycles. During the second cycle, the discharge capacity of the electrode is 331.0 mAh g^{-1} and capacity retention of around 82.3 % after 100 cycles.

To investigate the response of the OLDHC electrode at different currents, the cell was charged and discharged in the cycling rate from C/10 to 2C and back to C/10 between 0.01 and 3 V *vs.* Li^+ /Li. Fig. 4d shows the discharge capacity as a function of C-rate. The OLDHC electrode shows good rate capability at all C-rates, with reversible discharge capacity values of 350.0, 334.2, 315.6, 279.7, 235.8 mAh g^{-1} at C/10, C/5, C/2, 1C, and 2C, respectively.

To evaluate the kinetics of the charge/discharge processes and the interfacial behavior of the OLDHC electrode, electrochemical impedance spectroscopy (EIS) analysis was performed

every 10^{th} cycle at E = 0.5 V, at T = 25 °C, in the frequency range of 5 mHz to 100 kHz. The corresponding Nyquist plots are presented in Fig. 4e. All dispersions demonstrate common features: (i) an intercept on the real axis at highest frequencies correlated with electrolyte resistance; (ii) a high-frequency semicircle related to accumulation of charge at SEI surface and migration through it, which is partly overlapped by (iii) a medium-frequency semicircle correlated with electrical double layer formation and interfacial charge-transfer process; (iv) a sloped line at low frequencies corresponding to Li^+ ion diffusion to a blocking electrode [44]. The ac-impedance diagrams present comparable behaviors at 1^{st} and 10^{th} cycles. Form the 20^{th} cycle, different behavior and lower overall resistances, especially in the high-frequency region, are observed. This can be because of a rearrangement of the electrode/electrolyte interface due to the initial morphological instability [12]. The dispersions have been modelled with RelaxIS software (rhd instruments, Germany) via the equivalent circuit noted as R_{el} (R_{SEI} C_{SEI})($R_{ct}C_{dl}$) WC_i in the notation of Boukamp (inserted in Fig. 4f) [45]. R_{el}, R_{SEI}, C_{SEI}, R_{ct}, C_{dl}, W, C_i are the electrolyte resistance, the resistance and capacitance correlated with the passivation layer, the resistance of the charge-transfer process, the electrical double layer capacitance, the Warburg impedance and the intercalation capacitance, respectively [46]. Fig. 4f shows the overall trends of the calculated values of R_{el}, R_{SEI}, and R_{ct}. In order to take into account any inhomogeneities and roughness of the electrodes, during the fitting procedure, all the C elements have been substituted by constant-phase elements (CPE), marked as Q [47]. The R_{SEI} are initially high, then sharply decrease and finally increase again, due to initial rearrangement and then continuous growth of the electrode/electrolyte interface. The R_{ct} is initially decreasing and then almost constant upon cycling, indicating a stable charge transfer process at electrode surface. As regards electrolyte resistance, the calculated R_{el} values face a minor increase upon cycling.

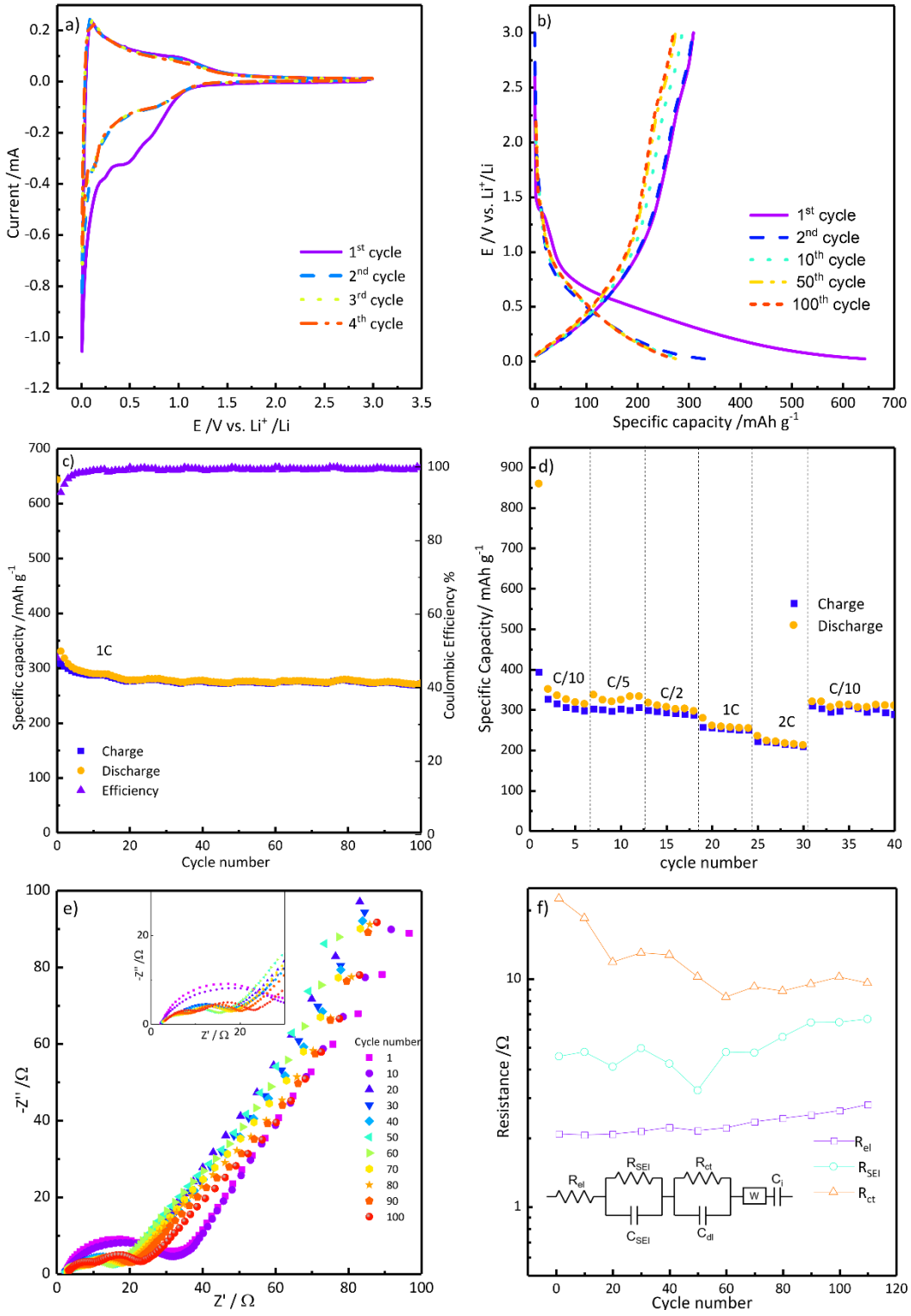

Fig. 4. Electrochemical performances of OLDHC-based LIB electrodes in the potential range of 0.01 – 3 V. (a) CV curves acquired during the first four cycles, scan rate 0.05 mV s^{-1}; (b) Galvanostatic discharge/charge voltage profiles obtained during the 1st, 2nd, 10th, 50th, 100th cycles at 1 C; (c) Cycling performances up to 100 cycles at 1 C; (d) Rate capability from C/10 to 2C and back to C/10; (e) Nyquist plot obtained every 10th cycle, E = 0.5 V, 10 mHz < f < 100 kHz; (f) Values of R_{el}, R_{SEI} and R_{ct} upon cycling, as acquired by EIS data analysis and Equivalent circuit used to simulate the data (insert).

For evaluating the diffusion behavior, the galvanostatic intermittent titration tests (GITT) serve as a powerful, tool linking charge kinetics and thermodynamics in insertion compounds. To achieve these, a GITT experiment was carried out at 0.1 C pulse current, 30 min pulse time, and a relaxation period of 2 h, between 0.01 and 3.0 V, and the apparent diffusion coefficient was calculated, as shown in Fig. 5a- d. Based on Fick's second law of diffusion, the diffusion coefficient of Li^+ (D_{Li+}) can be determined as following [7]:

$$D = \frac{4}{\pi\tau}\left(\frac{m_B V_m}{M_B S}\right)^2\left(\frac{\Delta E_s}{\Delta E_\tau}\right)^2$$

where τ is the pulse duration, V_m is the molar volume, m_B and M_B are, respectively, the active mass and molar mass of carbon employed, S is the active surface area of the electrode, ΔE_s is the OCV difference between two subsequent steps and ΔE_τ is the voltage difference generated by the current pulse. As shown in Fig. 5c, d, the Li^+ ions diffusion coefficient is in the range of 1-10 $\times 10^{-10}$ cm^2 s^{-1} during intercalation and deintercalation. The difference in the diffusion coefficient values in sloping and plateau regions reveals the presence of two different lithium storage mechanisms, according to the "adsorption- intercalation" model. Upon the lithiation process (Fig. 5c), the diffusion coefficient gradually decreases until the cut-off potential is reached. After the early stages of Li^+ ion storage, occurring by adsorption of Li^+ at unreacted carbon surface, further adsorption of Li^+ is energetically hindered by the presence of the previously adsorbed ions, thus resulting in hampered surface diffusion and slightly decreasing D values [38]. The steeper drop of Li^+ diffusion coefficient below 0.4 V can be ascribed by to the bulk solid-state diffusion of the intercalating Li^+ ions, which have now to overcome the repulsive forces due both to surface-preadsorbed and bulk-intercalated Li^+ ions. Upon delithiation (Fig. 5d), the diffusion coefficient first reduces until the voltage of about 0.1 V, then increases and finally decreases again until the cut-off potential [48]. The sharp decrease and increase of value at lower potential can be due to overcoming the repulsive forces from the interactions between the inserted ions and the surface in order to diffuse out from the

microcrystalline phase. Above 0.2 V, the value drops as the potential increases, representing the desorption of Li^+ ions from sites at progressively higher energy [31].

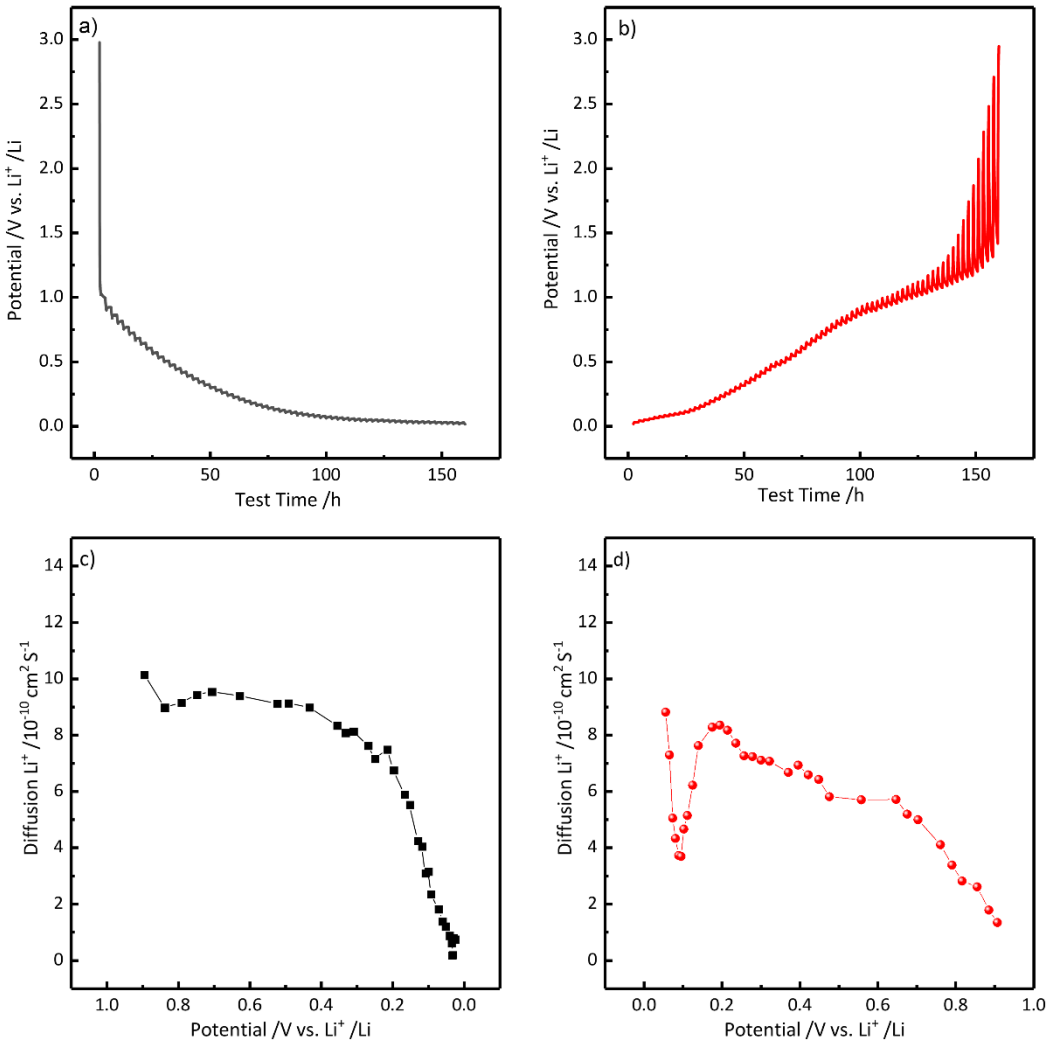

Fig. 5. GITT tests results of OLDHC-based LIB electrode at 0.1 C pulse current, 30 min pulse time, and a relaxation period of 2 h. Li^+ intercalation (a) and deintercalation (b) upon the second cycle; Li^+ apparent diffusion coefficients obtained from GITT during Li^+ intercalation (c) and deintercalation (d).

3.3 Sodium storage performance

As for LIBs, OLDHC can be utilized as NIBs candidate anode material as well. To explore the Na^+-storage properties of the ball-milled OLDHC electrode, electrochemical measurements were carried out in the potential window of 0.01-3.00 V in half cells *vs.* Na^+ /Na. Fig. 6a shows the CV curve at the initial four cycles at a scan rate of 0.05 mV s^{-1}. Discharging voltage plateaus can be observed at initial cycle, disappearing at the following cycles. This feature reveals the

first irreversible sodiation capacity and results into low initial coulombic efficiency, which is due to SEI formation and electrolyte decomposition [37]. During all the cathodic and anodic scans, the intense redox peaks around 0.01 V can be assigned to reversible Na^+ ions insertion/ extraction involving the hard carbon structure [49]. Galvanostatic E vs. Q profiles at 1C are presented in Fig. 6b, while Fig. 6c reports the charge/discharge capacity values upon cycling, together with the calculated Coulombic efficiency. The anode exhibits a specific capacity of 435.8 mAh g^{-1} and a Coulombic efficiency around 52.4% during the initial cycle. The discharge capacity of the electrode is 265.37 mAh g^{-1} at 1C during the second cycle (comparable or even superior to those reported in the literature, see table S1), and minor irreversibility can be seen up to the fifth cycle. Afterwards, the reversible capacity stabilizes at around 200 mAh g^{-1}, with Coulombic efficiency of 99.7% and capacity retention of around 71.7% after 100 cycles. The initial irreversible capacity and low initial coulombic efficiency confirm the CV results. The response of the OLDHC electrode at different currents was also investigated for NIBs and the cell was discharged and charged in the cycling rate from C/10 to 2C, and back to C/10, between 0.01 and 3 V *vs*. Na^+ /Na. Fig. 6d presents the discharge capacity as a function of C-rate. The electrode delivers promising rate capability at all C-rates, with a reversible discharge capacity of 294.8, 270.2, 242.7, 222.5, 178.8 mAh g^{-1} at C/10, C/5, C/2, 1C, and 2C, respectively. However, the cell shows the low Coulombic efficiency at C/10, which can be due to high surface reactivity toward slow-kinetics electrolyte decomposition. The OLDHC electrodes were also charged and discharged at high C-rate (5C) up to 100 cycles and the electrode shows high specific capacities of around 150 and 300 mAh g^{-1} for NIBs and LIBs, respectively, as shown in Fig. S4. Besides, in order to evaluate the effect of ball milling and particle size on the electrochemical performance, the cells based on not ball-milled OLDHC active material, were charged and discharged at 1C in the potential window of 0.01-3.00 V (see Fig S5). The OLDHC-based (without ball-milling) LIB electrode shows a specific capacity of 325.14 mAh

g^{-1} with a capacity retention of 64% after 100 cycles (Fig. S5a), which is lower than those for the ball-milled OLDHC-based electrode. Regarding NIBs, the ball-milled OLDHC-based electrode demonstrates a higher specific capacity and more stable cycling compared to not ball-milled OLDHC electrode (specific capacity of 225.32 mAh g^{-1}), observed in Fig. S5b. Therefore, as expected, reducing particle size and hindering particles from aggregating have a considerable impact on the electrochemical performance by expanding the active material/electrolyte interfacial area and decreasing the solid-state ion diffusion pathways during cycling. The performances obtained in this work, are comparable or even superior to those reported in the literature for hard carbon electrodes for both LIBs and NIBs, shown in Table 1.

To evaluate interfacial properties EIS characterization was carried out for each tenth cycle at E = 0.5 V for NIBs as well. The Nyquist plots are presented in Fig. 6e. The semicircle in the high frequency area outcomes from the SEI resistance (R_{SEI}) and charge transfer impedance charge (R_{ct}) at the electrode/electrolyte interface, while the line in the low-frequency region results from the Warburg impedance (W), which comes from the diffusion of the Na^+ ions in the electrode material. Upon the first cycle, a different behavior is revealed compared to subsequent cycles, which can be due to activation of the electrode [12]. The dispersions were fitted with the same equivalent circuit proposed for LIBs and the results are shown in Fig. 6f. Both R_{el} and R_{SEI} values face slight oscillations and show an increasing trend upon cycling. Higher resistance values are associated with charge-transfer processes. The R_{ct} is high during the first cycle, and almost constant for the following cycles, confirming the interfacial behavior stability of the electrode.

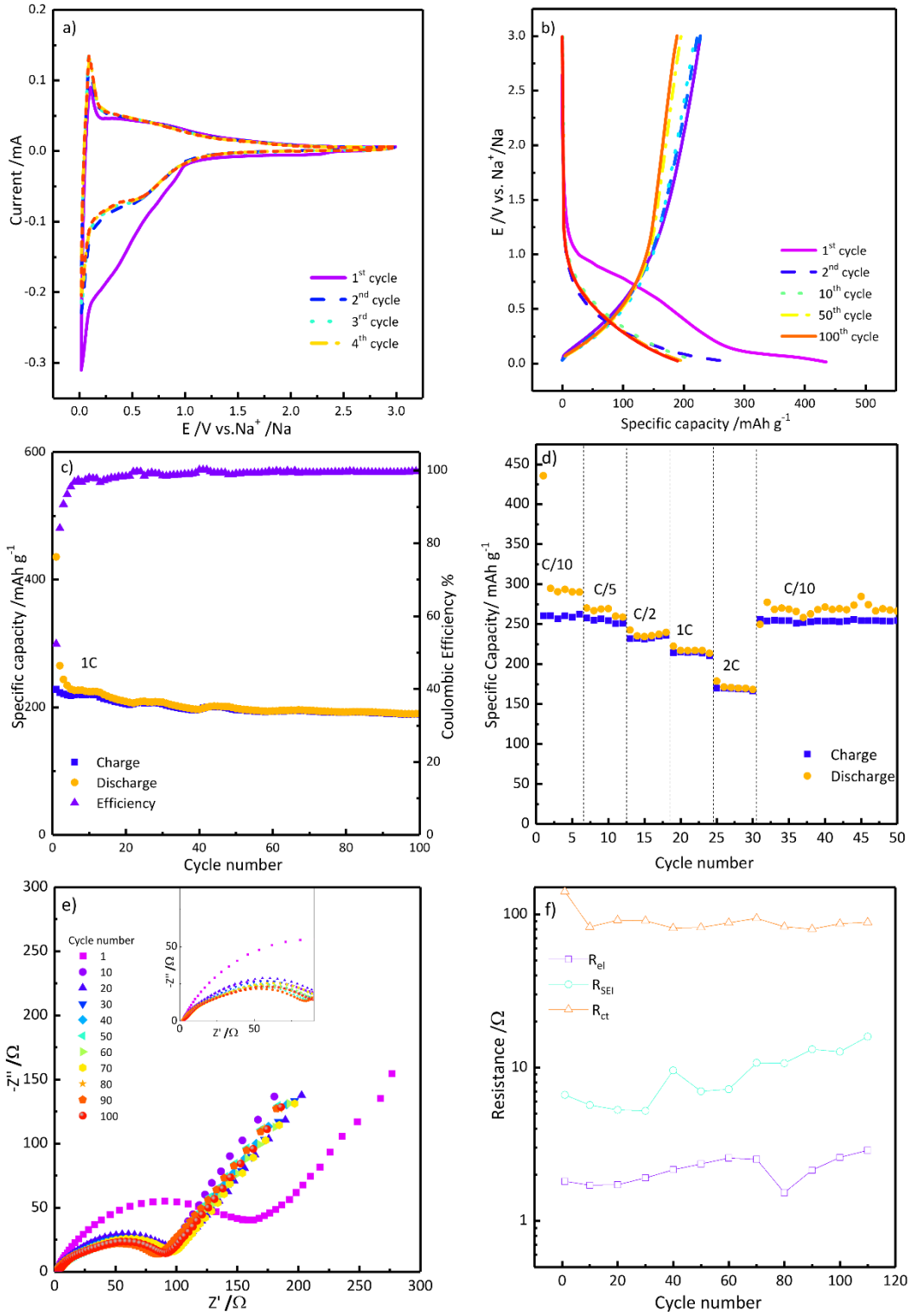

Fig. 6. Electrochemical performances of OLDHC-based NIB electrode in the potential range of 0.01 – 3 V. (a) CV curves acquired during the first four cycles, scan rate 0.05 mV s^{-1}; (b) Galvanostatic discharge/charge voltage profiles obtained during the 1st, 2nd, 10th, 50th, 100th cycles at 1 C; (c) Cycling performances up to 100 cycles at 1 C; (d) Rate capability from C/10 to 2C and back to C/10; (e) Nyquist plot obtained every 10th cycle, E = 0.5 V, 10 mHz < f < 100 kHz.; (f) Values of R_{el}, R_{SEI} and R_{ct} upon cycling, as acquired by EIS data analysis.

Table 1. Selected overview of literature on hard carbon electrochemical performances for sodium-ion/lithium-ion batteries.

Precursor	**Binder**	**Specific Capacity for LIBs ($mAhg^{-1}$)**	**Specific Capacity for NIBs ($mAhg^{-1}$)**	**Current density (mAg^{-1})**	**Refs.**
Unburned charcoal-Derived HC	Na-CMC	350	150	100	[48]
Olive pits-Derived HC	PVDF	290	243	30	[27]
N-doped HC	PVDF	389 after 100 cycles	136 after 100 cycles	100	[50]
Tires-Derived HC	Teflon	290	140	30	[51]
D-glucose-Derived HC	PVDF	400	175 at 0.1 V vs Na/Na^+ and 330 at 1.5 V vs Na/Na^+	25	[52]
Coffee ground-Derived HC	CMC	421	173	60	[12]
Peanut shells-Derived HC	PVDF	474	193	1000 for LIBs and 250 for NIBs	[23]
Bamboo leaves-Derived HC	Na-CMC	600	200	200 for LIBs and 100 for NIBs	[31]
HC, Kuraray, Japan	Na-CMC	220	280	30	[53]
Olive leaves-Derived HC	Na-CMC	331 and 300	265 and 150	300 and 1500, respectively.	**This work**

Fig. 7a-d shows the GITT curves of NIBs at 0.1 C pulse current (30 min pulse time, and a relaxation period of 2 h between 0.01 and 3.0 V) and the obtained apparent diffusion coefficient. As can be observed in Fig. 7c, d, the Na^+ ions diffusivity coefficient is in the range of 1-4.5 $\times 10^{-10}$ cm^2 s^{-1} upon the sodiation and desodiation, representing the fast diffusion of Na^+, which results in a good rate capability. Upon the sodiation process (Fig. 7c), the diffusion coefficient first decreases, then slightly increases, decreases again and finally increases. In the desodiation process (Fig. 7d), the diffusion coefficient first declines until 0.10 V, and then increases followed by decreasing again before the cut-off voltage. The difference in the diffusion coefficient values in sloping and plateau regions reveals the presence of two different sodium storage mechanisms according to the "adsorption- intercalation" model. During

sodiation, higher Na^+ ions diffusion coefficient values are evidenced in the potential sloping region extending down to 0.1 V, which corresponds to the adsorption of Na^+ ions on the surface-active sites, such as micropore surface, edge, defects, of the hard carbons due to the easy accessibility of Na^+ ions [38]. The next step is the intercalation of alkaline ions between the layers, resulting in considerable drop of ions diffusivity. As mentioned for LIBs, this can be due to overcoming the repulsive forces from the interactions between the inserted ions and the surface to diffuse into the microcrystalline phase.

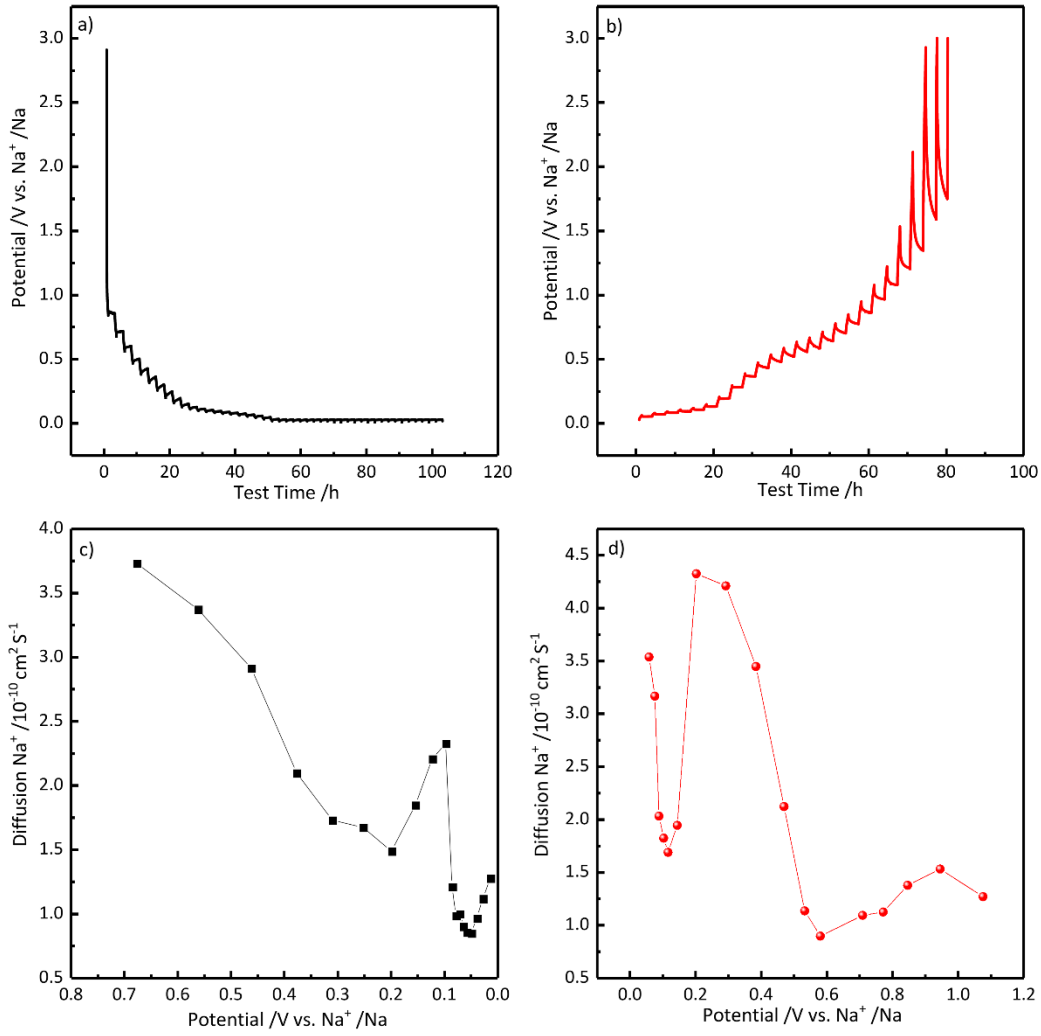

Fig. 7. GITT tests results of OLDHC-based NIB electrode at 0.1 C pulse current, 30 min pulse time, and a relaxation period of 2 h. Sodiation (a) and desodiation (b) upon the second cycle; Na^+ apparent diffusion coefficients obtained from GITT during sodiation (c) and desodiation (d).

Double layer capacitive performance

To investigate the electrochemical performances of the OLDHC for supercapacitor, a three-electrode system was utilized in a 6 M KOH aqueous electrolyte under the potential range of -1.2 - 0 V *vs.* SCE, as shown in Fig. 8a-d. The CVs of the electrode (Fig. 8a) at various scanning rates of 2, 5, 10, 25, 50, 75, and 100 mV s^{-1} display a quasi-rectangular shape with no significant distortion. This demonstrates the outstanding charge diffusion, a high reversible capacitance, good rate capability, and stability [54,55], which can be explained by the shortening of ion diffusion pathways due to the high porosity of the material [22]. Besides, all CV curves show no Faradaic peaks, demonstrating the predominant role of the electrostatic charge storage mechanism [55].

The galvanostatic charge/discharge (GCD) curves of the electrode at different current densities of 0.5, 1, 2, 3, 5, 8, and 10 A g^{-1} exhibit nearly symmetric triangular shape without IR drop (Fig. 8b), representing EDLC behavior and excellent reversibility of capacitive charge storage [35]. The specific capacitances (SC) versus different current densities ranging from 0.5 to 10 A g^{-1} are given in Fig. 8c, which are calculated by the following equation 1:

$$SC = \frac{I\Delta t}{m\Delta V} \quad (1)$$

Where I is the discharge current (A), Δt is the discharge time (s), ΔV is the potential window (V), and m is the mass of electro-active material (g) [56]. The calculated SC values from GCD curves are 169.6, 147.5, 135.1, 125, 120.4, 110.3, 104.2 F g^{-1} at current densities of 0.5, 1, 2, 3, 5, 8, and 10 A g^{-1}, respectively. The performances shown herein are comparable or even higher than those reported in recent literature for hard carbon electrodes in comparable current ranges (Table 2).

To shed light on the charge storage kinetics and electrolyte ion diffusion properties, EIS measurements were carried out at a frequency range of 10 mHz to 100 kHz with an AC amplitude of 10 mV. The results are shown in Fig. 8d. The Nyquist plot is composed of two

parts: low-frequency straight line (W), which corresponds to the ion diffusion limitation, and high-frequency semicircle, which relates to the charge-transfer resistance (R_{ct}) [35]. Besides, the intercept of the R_{ct} semicircle along the *Z'* axis at high frequency represents the bulk resistance of the electrolyte solution (R_s). The diameter of the quasi-semicircle reveals the value of R_{ct}, which is less than 0.25 Ω (insert of Fig. 8d). The shape of the semicircle confirms the presence of heteroatoms, evidenced by XPS, which may have surface redox activity with electrolyte ions [55,57]. The R_{ct} and R_s values are much lower compared to other literature findings [55], evidencing low internal resistance, promising ionic conductivity, as well as fast adsorption-desorption kinetics. The relatively steep slope of the line at low frequencies reveals that the electric double layers are easy to establish.

Long cycle life plays a vital role in the electrochemical capacitor [58,59]. Fig. 8e presents the cyclic stability of OLDHC at a current density of 10 A g^{-1}, which maintains 96.7 % of its initial capacitance after more than 20,000 cycles. The excellent capacity retention of the electrode can be assigned to the appropriate microporous structure, simplifying ion diffusion pathways for rapid electrolyte ions transportation and fast generation of the electric double layers [60].

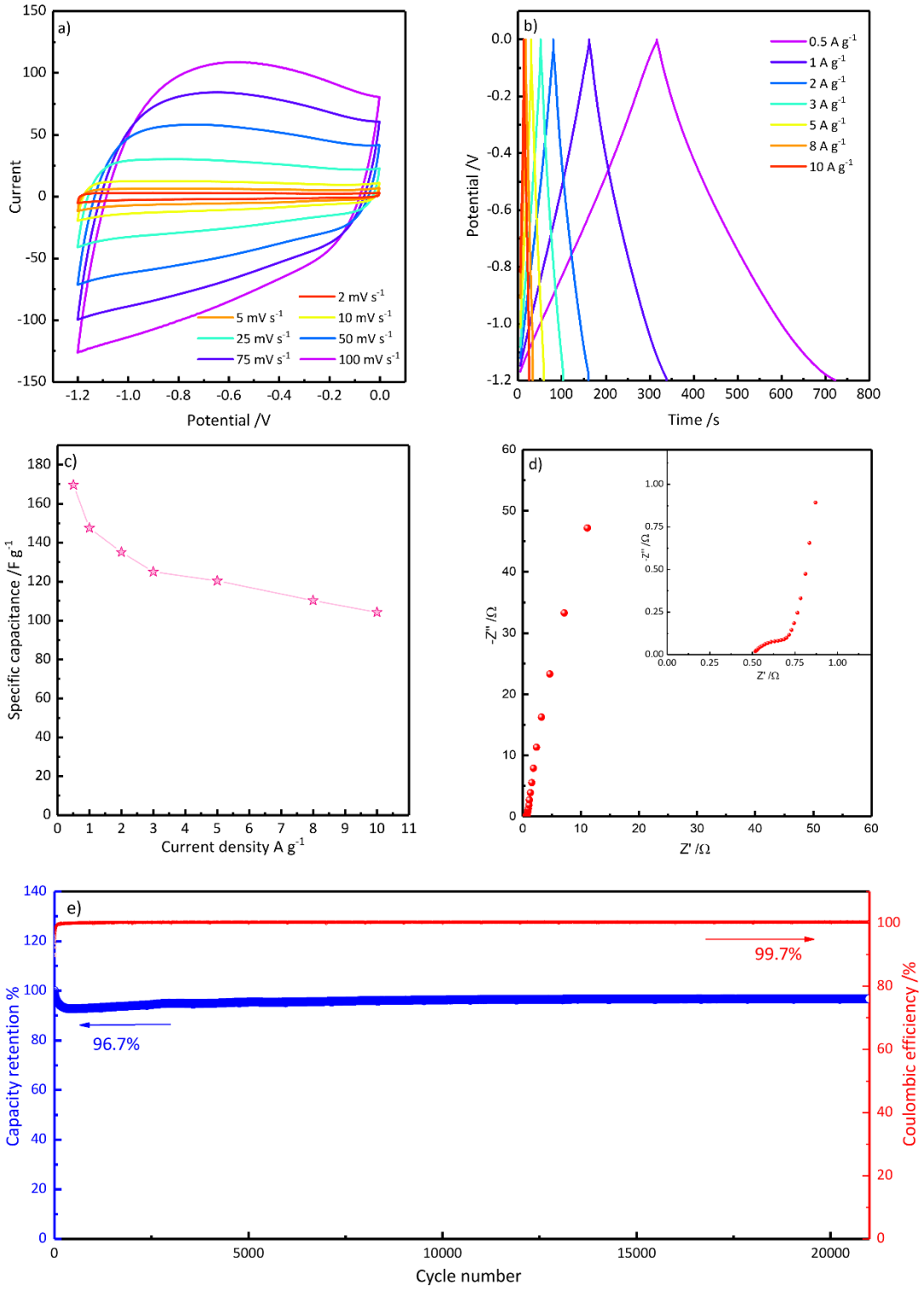

Fig. 8. Electrochemical performance of OLDHC in 6 M KOH aqueous electrolyte in the potential range of -1.2 – 0 V *vs.* SCE in a three-electrode system. (a) CV curves tested at the scan rates of 2, 5, 10, 25, 50, 75, and 100 mV s^{-1}. (b) Galvanostatic charge/discharge curves measured at current densities of 0.5, 1, 2, 3, 5, 8, and 10 A g^{-1}. (c) The specific capacitance versus different current densities. (d) The Nyquist plots. (e) Cycling stability and Coulombic efficiency after more than 20000 cycles, measured at a current density of 10 A g^{-1}.

Table 2. Selected literature overview of performance of waste derived carbon as electrode for EDLCs.

Electrode materials	Current densities ($A\ g^{-1}$)	Electrolyte	Specific capacitance ($F\ g^{-1}$)	Cycle number	Cycling stability	Reference
Tea waste derived (co doping)	0.5	KOH	170	14,000	94.8%	[55]
Tobacco Waste	0.5	KOH	148	9,000	100%	[61]
Kraft Lignin	1	KOH	~190	10,000	~ 92%	[62]
Cigarette filter derived	1	KOH	153.8	6,000	Slight increase	[57]
Shrimp shells	0.5	KOH	175	1,000	94%	[63]
Olive-leaves derived	0.5	KOH	169.7	21,000	96.7%	This work

4. Conclusions

In this work, we synthesized a cost-efficient hard carbon that was derived from olive leaf waste for use as an active material for electrodes in LIBs, NIBs, and SCs. For LIBs applications, the electrode exhibited a large reversible initial specific capacity of 331.02 mAh g^{-1} and stability of 82% over 100 cycles. The electrochemical results for NIBs reveal that the electrode is capable of delivering a high discharge capacity of 265.37 mAh g^{-1} during the second cycle and cycling stability of about 71.7% after 100 cycles with coulombic efficiency of 99.7%. At the same time, as a supercapacitor electrode, 96.7 % of the initial specific capacitance can be retained after more than 20,000 cycles due to the suitable microporous structure. The good electrochemical performances, coupled with the sustainable circular economy approach, make

the reported olive leaves-derived hard carbon suitable and promising electrode material for LIBs, NIBs, and SCs.

Acknowledgments: This research was funded by ENEA (Agenzia Nazionale per le Nuove Tecnologie, l'Energia e lo Sviluppo Sostenibile) and MiSE (Ministero per lo Sviluppo Economico). Project: 'Sistemi di Accumulo di Energia per il Sistema Elettrico' in the framework of 2019-2021 PTR Program of ENEA/MiSE. This work was also partly funded within the FAR (Fondi di Ateneo per la Ricerca) framework of the University of Camerino. Project: "yielding added valuE to Apennine Forest resources (LEAF)".

References

1. Wang, G.; Zhang, L.; Zhang, J. A review of electrode materials for electrochemical supercapacitors. *Chem. Soc. Rev.* **2012**, *41*, 797–828, doi:10.1039/c1cs15060j.
2. Liu, Y.; Liu, X.; Wang, T.; Fan, L.Z.; Jiao, L. Research and application progress on key materials for sodium-ion batteries. *Sustain. Energy Fuels* **2017**, *1*, 986–1006, doi:10.1039/c7se00120g.
3. Kim, S.W.; Seo, D.H.; Ma, X.; Ceder, G.; Kang, K. Electrode materials for rechargeable sodium-ion batteries: Potential alternatives to current lithium-ion batteries. *Adv. Energy Mater.* **2012**, *2*, 710–721, doi:10.1002/aenm.201200026.
4. Darjazi, H.; Rezvani, S.J.; Brutti, S.; Nobili, F. Improvement of structural and electrochemical properties of NMC layered cathode material by combined doping and coating. *Electrochim. Acta* **2021**, 139577, doi:10.1016/j.electacta.2021.139577.
5. Hou, Z.; Xia, S.; Niu, C.; Pang, Y.; Sun, H.; Li, Z.; Xu, Y.; Zheng, S. Tailoring the interaction of covalent organic framework with the polyether matrix toward high-performance solid-state lithium metal batteries. *Carbon Energy* **2022**, 506–516, doi:10.1002/cey2.190.
6. Darjazi, H.; Gonzalo, E.; Acebedo, B.; Cid, R.; Zarrabeitia, M.; Bonilla, F.; Muñoz-Márquez, M.Á.; Nobili, F. Improving High-voltage Cycling Performance of Nickel-rich NMC Layered Oxide Cathodes for Rechargeable Lithium-ion Batteries by Mg and Zr co-doping. *Mater. Today Sustain.* **2022**, *20*, 100236, doi:10.1016/j.mtsust.2022.100236.
7. Li, Y.; Hu, Y.S.; Titirici, M.M.; Chen, L.; Huang, X. Hard Carbon Microtubes Made from Renewable Cotton as High-Performance Anode Material for Sodium-Ion Batteries. *Adv. Energy Mater.* **2016**, *6*, doi:10.1002/aenm.201600659.
8. Hong, S.Y.; Kim, Y.; Park, Y.; Choi, A.; Choi, N.S.; Lee, K.T. Charge carriers in rechargeable batteries: Na ions vs. Li ions. *Energy Environ. Sci.* **2013**, *6*, 2067–2081,

doi:10.1039/c3ee40811f.

9. Zhao, Y.; Ruan, J.; Luo, S.; Sun, H.; Pang, Y.; Yang, J.; Zheng, S. Rational Construction of a Binder-Free and Universal Electrode for Stable and Fast Alkali-Ion Storage. *ACS Appl. Mater. Interfaces* **2019**, *1*, doi:10.1021/acsami.9b13889.
10. Majid, S.; Ali, A.S.G.; Cao, W.Q.; Reza, R.; Ge, Q. Biomass-derived porous carbons as supercapacitor electrodes-A review. *Xinxing Tan Cailiao/New Carbon Mater.* **2021**, *36*, 546–572, doi:10.1016/S1872-5805(21)60038-0.
11. Dou, X.; Hasa, I.; Saurel, D.; Vaalma, C.; Wu, L.; Buchholz, D.; Bresser, D.; Komaba, S.; Passerini, S. Hard carbons for sodium-ion batteries: Structure, analysis, sustainability, and electrochemistry. *Mater. Today* **2019**, *23*, 87–104, doi:10.1016/j.mattod.2018.12.040.
12. Darjazi, H.; Staffolani, A.; Sbrascini, L.; Bottoni, L.; Tossici, R.; Nobili, F. Sustainable Anodes for Lithium- and Sodium-Ion Batteries Based on Coffee Ground-Derived Hard Carbon and Green Binders. *Energies* **2020**, *13*, 6216, doi:10.3390/en13236216.
13. Saurel, D.; Orayech, B.; Xiao, B.; Carriazo, D.; Li, X.; Rojo, T. From Charge Storage Mechanism to Performance: A Roadmap toward High Specific Energy Sodium-Ion Batteries through Carbon Anode Optimization. *Adv. Energy Mater.* **2018**, *8*, 1–33, doi:10.1002/aenm.201703268.
14. Liu, P.; Li, Y.; Hu, Y.S.; Li, H.; Chen, L.; Huang, X. A waste biomass derived hard carbon as a high-performance anode material for sodium-ion batteries. *J. Mater. Chem. A* **2016**, *4*, 13046–13052, doi:10.1039/c6ta04877c.
15. Lotfabad, E.M.; Ding, J.; Cui, K.; Kohandehghan, A.; Kalisvaart, W.P.; Hazelton, M.; Mitlin, D. High-density sodium and lithium ion battery anodes from banana peels. *ACS Nano* **2014**, *8*, 7115–7129, doi:10.1021/nn502045y.
16. Wu, L.; Buchholz, D.; Vaalma, C.; Giffin, G.A.; Passerini, S. Apple-Biowaste-Derived

Hard Carbon as a Powerful Anode Material for Na-Ion Batteries. *ChemElectroChem* **2016**, *3*, 292–298, doi:10.1002/celc.201500437.

17. Beda, A.; Taberna, P.; Simon, P.; Ghimbeu, C.M.; Beda, A.; Taberna, P.; Simon, P.; Matei, C.; Hard, G. Hard carbons derived from green phenolic resins for Na-ion batteries To cite this version : HAL Id : hal-02022742. **2019**.
18. Kim, N.R.; Yun, Y.S.; Song, M.Y.; Hong, S.J.; Kang, M.; Leal, C.; Park, Y.W.; Jin, H.J. Citrus-peel-derived, nanoporous carbon nanosheets containing redox-active heteroatoms for sodium-ion storage. *ACS Appl. Mater. Interfaces* **2016**, *8*, 3175–3181, doi:10.1021/acsami.5b10657.
19. Ding, J.; Wang, H.; Li, Z.; Kohandehghan, A.; Cui, K.; Xu, Z.; Zahiri, B.; Tan, X.; Lotfabad, E.M.; Olsen, B.C.; et al. Carbon nanosheet frameworks derived from peat moss as high performance sodium ion battery anodes. *ACS Nano* **2013**, *7*, 11004–11015, doi:10.1021/nn404640c.
20. Wang, L.; Schnepp, Z.; Titirici, M.M. Rice husk-derived carbon anodes for lithium ion batteries. *J. Mater. Chem. A* **2013**, *1*, 5269–5273, doi:10.1039/c3ta10650k.
21. Li, Y.; Paranthaman, M.P.; Akato, K.; Naskar, A.K.; Levine, A.M.; Lee, R.J.; Kim, S.O.; Zhang, J.; Dai, S.; Manthiram, A. Tire-derived carbon composite anodes for sodium-ion batteries. *J. Power Sources* **2016**, *316*, 232–238, doi:10.1016/j.jpowsour.2016.03.071.
22. Zhao, C.; Huang, Y.; Zhao, C.; Shao, X.; Zhu, Z. Rose-derived 3D carbon nanosheets for high cyclability and extended voltage supercapacitors. *Electrochim. Acta* **2018**, *291*, 287–296, doi:10.1016/j.electacta.2018.09.136.
23. Lv, W.; Wen, F.; Xiang, J.; Zhao, J.; Li, L.; Wang, L.; Liu, Z.; Tian, Y. Peanut shell derived hard carbon as ultralong cycling anodes for lithium and sodium batteries. *Electrochim. Acta* **2015**, *176*, 533–541, doi:10.1016/j.electacta.2015.07.059.
24. Li, Y.; Hu, Y.S.; Li, H.; Chen, L.; Huang, X. A superior low-cost amorphous carbon

anode made from pitch and lignin for sodium-ion batteries. *J. Mater. Chem. A* **2015**, *4*, 96–104, doi:10.1039/c5ta08601a.

25. Li, H.; Shen, F.; Luo, W.; Dai, J.; Han, X.; Chen, Y.; Yao, Y.; Zhu, H.; Fu, K.; Hitz, E.; et al. Carbonized-leaf Membrane with Anisotropic Surfaces for Sodium-ion Battery. *ACS Appl. Mater. Interfaces* **2016**, *8*, 2204–2210, doi:10.1021/acsami.5b10875.

26. Xiang, J.; Lv, W.; Mu, C.; Zhao, J.; Wang, B. Activated hard carbon from orange peel for lithium/sodium ion battery anode with long cycle life. *J. Alloys Compd.* **2017**, *701*, 870–874, doi:10.1016/j.jallcom.2017.01.206.

27. Ajuria, J.; Redondo, E.; Arnaiz, M.; Mysyk, R.; Rojo, T.; Goikolea, E. Lithium and sodium ion capacitors with high energy and power densities based on carbons from recycled olive pits. *J. Power Sources* **2017**, *359*, 17–26, doi:10.1016/j.jpowsour.2017.04.107.

28. Ni, J.; Huang, Y.; Gao, L. A high-performance hard carbon for Li-ion batteries and supercapacitors application. *J. Power Sources* **2013**, *223*, 306–311, doi:10.1016/j.jpowsour.2012.09.047.

29. Xu, Y.; Ruan, J.; Pang, Y.; Sun, H.; Liang, C.; Li, H.; Yang, J.; Zheng, S. Homologous Strategy to Construct High-Performance Coupling Electrodes for Advanced Potassium-Ion Hybrid Capacitors. *Nano-Micro Lett.* **2021**, *13*, 1–14, doi:10.1007/s40820-020-00524-z.

30. Yield, B.; State, C. Insight into Pretreatment Methods of Lignocellulosic Biomass to Increase applied sciences Insight into Pretreatment Methods of Lignocellulosic Biomass to Increase Biogas Yield : Current State , Challenges , and Opportunities. **2019**, doi:10.3390/app9183721.

31. Yan, Z.; Yang, Q.W.; Wang, Q.; Ma, J. Nitrogen doped porous carbon as excellent dual anodes for Li- and Na-ion batteries. *Chinese Chem. Lett.* **2020**, *31*, 583–588,

doi:10.1016/j.cclet.2019.11.002.

32. Velez, V.; Ramos-Sánchez, G.; Lopez, B.; Lartundo-Rojas, L.; González, I.; Sierra, L. Synthesis of novel hard mesoporous carbons and their application as anodes for Li and Na ion batteries. *Carbon N. Y.* **2019**, *147*, 214–226, doi:10.1016/j.carbon.2019.02.083.

33. Wu, Z.; Zou, J.; Zhang, Y.; Lin, X.; Fry, D.; Wang, L.; Liu, J. Lignin-derived hard carbon anode for potassium-ion batteries: Interplay among lignin molecular weight, material structures, and storage mechanisms. *Chem. Eng. J.* **2022**, *427*, 131547, doi:10.1016/j.cej.2021.131547.

34. Zhu, X.; Jiang, X.; Liu, X.; Xiao, L.; Cao, Y. A green route to synthesize low-cost and high-performance hard carbon as promising sodium-ion battery anodes from sorghum stalk waste. *Green Energy Environ.* **2017**, *2*, 310–315, doi:10.1016/j.gee.2017.05.004.

35. Liu, Z.; Qin, A.; Zhang, K.; Lian, P.; Yin, X.; Tan, H. Design and structure of nitrogen and oxygen co-doped carbon spheres with wrinkled nanocages as active material for supercapacitor application. *Nano Energy* **2021**, *90*, 106540, doi:10.1016/j.nanoen.2021.106540.

36. Moon, H.; Zarrabeitia, M.; Frank, E.; Böse, O.; Enterría, M.; Saurel, D.; Hasa, I.; Passerini, S. Assessing the Reactivity of Hard Carbon Anodes: Linking Material Properties with Electrochemical Response Upon Sodium- and Lithium-Ion Storage. *Batter. Supercaps* **2021**, *4*, 960–977, doi:10.1002/batt.202000322.

37. Muruganantham, R.; Hsieh, T.H.; Lin, C.H.; Liu, W.R. Bio-oil derived hierarchical porous hard carbon from rubber wood sawdust via a template fabrication process as highly stable anode for sodium-ion batteries. *Mater. Today Energy* **2019**, *14*, 100346, doi:10.1016/j.mtener.2019.100346.

38. Alvin, S.; Cahyadi, H.S.; Hwang, J.; Chang, W.; Kwak, S.K.; Kim, J. Revealing the Intercalation Mechanisms of Lithium, Sodium, and Potassium in Hard Carbon. *Adv.*

Energy Mater. **2020**, *10*, 1–16, doi:10.1002/aenm.202000283.

39. Stevens, D.A.; Dahn, J.R. High Capacity Anode Materials for Rechargeable Sodium-Ion Batteries. *J. Electrochem. Soc.* **2000**, *147*, 1271, doi:10.1149/1.1393348.
40. Stevens, D.A.; Dahn, J.R. The Mechanisms of Lithium and Sodium Insertion in Carbon Materials. *J. Electrochem. Soc.* **2001**, *148*, A803, doi:10.1149/1.1379565.
41. Ghani, U.; Iqbal, N.; Aboalhassan, A.A.; Liu, B.; Aftab, T.; Zada, I.; Ullah, F.; Gu, J.; Li, Y.; Zhu, S.; et al. One-step sonochemical fabrication of biomass-derived porous hard carbons; towards tuned-surface anodes of sodium-ion batteries. *J. Colloid Interface Sci.* **2022**, *611*, 578–587, doi:10.1016/j.jcis.2021.12.104.
42. Fan, Q.; Zhang, W.; Duan, J.; Hong, K.; Xue, L.; Huang, Y. Effects of binders on electrochemical performance of nitrogen-doped carbon nanotube anode in sodium-ion battery. *Electrochim. Acta* **2015**, *174*, 970–977, doi:10.1016/j.electacta.2015.06.039.
43. Hou, H.; Shao, L.; Zhang, Y.; Zou, G.; Chen, J.; Ji, X. Large-Area Carbon Nanosheets Doped with Phosphorus: A High-Performance Anode Material for Sodium-Ion Batteries. *Adv. Sci.* **2017**, *4*, doi:10.1002/advs.201600243.
44. Nobili, F.; Dsoke, S.; Mancini, M.; Tossici, R.; Marassi, R. Electrochemical investigation of polarization phenomena and intercalation kinetics of oxidized graphite electrodes coated with evaporated metal layers. *J. Power Sources* **2008**, *180*, 845–851, doi:10.1016/j.jpowsour.2008.02.069.
45. Boukamp, B.A. A Nonlinear Least Squares Fit procedure for analysis of immittance data of electrochemical systems. *Solid State Ionics* **1986**, *20*, 31–44, doi:10.1016/0167-2738(86)90031-7.
46. Feng, J.; Wang, L.; Li, D.; Lu, P.; Hou, F.; Liang, J. Enhanced electrochemical stability of carbon-coated antimony nanoparticles with sodium alginate binder for sodium-ion batteries. *Prog. Nat. Sci. Mater. Int.* **2018**, *28*, 205–211,

doi:10.1016/j.pnsc.2018.01.018.

47. Macdonald, J.R.; Wiley, a J. *Theory , Experiment , and*; ISBN 9786468600.

48. Yu, H.Y.; Liang, H.J.; Gu, Z.Y.; Meng, Y.F.; Yang, M.; Yu, M.X.; Zhao, C. De; Wu, X.L. Waste-to-wealth: low-cost hard carbon anode derived from unburned charcoal with high capacity and long cycle life for sodium-ion/lithium-ion batteries. *Electrochim. Acta* **2020**, *361*, 137041, doi:10.1016/j.electacta.2020.137041.

49. Beda, A.; Le Meins, J.M.; Taberna, P.L.; Simon, P.; Matei Ghimbeu, C. Impact of biomass inorganic impurities on hard carbon properties and performance in Na-ion batteries. *Sustain. Mater. Technol.* **2020**, *26*, doi:10.1016/j.susmat.2020.e00227.

50. Wang, N.; Liu, Q.; Sun, B.; Gu, J.; Yu, B.; Zhang, W.; Zhang, D. N-doped catalytic graphitized hard carbon for high-performance lithium/sodium-ion batteries. *Sci. Rep.* **2018**, *8*, 1–8, doi:10.1038/s41598-018-28310-3.

51. Dell'Era, A.; Pasquali, M.; Tarquini, G.; Scaramuzzo, F.A.; De Gasperis, P.; Prosini, P.P.; Mezzi, A.; Tuffi, R.; Cafiero, L. Carbon powder material obtained from an innovative high pressure water jet recycling process of tires used as anode in alkali ion (Li, Na) batteries. *Solid State Ionics* **2018**, *324*, 20–27, doi:10.1016/j.ssi.2018.06.008.

52. Väli, R.; Jänes, A.; Thomberg, T.; Lust, E. Synthesis and characterization of D-glucose derived nanospheric hard carbon negative electrodes for lithium- and sodium-ion batteries. *Electrochim. Acta* **2017**, *253*, 536–544, doi:10.1016/j.electacta.2017.09.094.

53. Linsenmann, F.; Pritzl, D.; Gasteiger, H.A. Comparing the Lithiation and Sodiation of a Hard Carbon Anode Using In Situ Impedance Spectroscopy. *J. Electrochem. Soc.* **2021**, *168*, 010506, doi:10.1149/1945-7111/abd64e.

54. Mu, J.; Wong, S.I.; Li, Q.; Zhou, P.; Zhou, J.; Zhao, Y.; Sunarso, J.; Zhuo, S. Fishbone-derived N-doped hierarchical porous carbon as an electrode material for supercapacitor. *J. Alloys Compd.* **2020**, *832*, 154950, doi:10.1016/j.jallcom.2020.154950.

55. Ma, Q.; Xi, H.; Cui, F.; Zhang, J.; Chen, P.; Cui, T. Self-templating synthesis of hierarchical porous carbon with multi-heteroatom co-doping from tea waste for high-performance supercapacitor. *J. Energy Storage* **2021**, 103509, doi:10.1016/j.est.2021.103509.

56. Ameri, B.; Davarani, S.S.H.; Moazami, H.R.; Darjazi, H. Cathodic electrosynthesis of $ZnMn_2O_4/Mn_3O_4$ composite nanostructures for high performance supercapacitor applications. *J. Alloys Compd.* **2017**, *720*, 408–416, doi:10.1016/j.jallcom.2017.05.271.

57. Lee, M.; Kim, G.P.; Don Song, H.; Park, S.; Yi, J. Preparation of energy storage material derived from a used cigarette filter for a supercapacitor electrode. *Nanotechnology* **2014**, *25*, doi:10.1088/0957-4484/25/34/345601.

58. Moazami, H.R.; Davarani, S.S.H.; Yousefi, T.; Darjazi, H. Iron mediated cathodic electrosynthesis of hausmannite nanoparticles. *Mater. Sci. Semicond. Process.* **2015**, *38*, 240–248, doi:10.1016/j.mssp.2015.04.035.

59. Darjazi, H.; Hosseiny Davarani, S.S.; Moazami, H.R.; Yousefi, T.; Tabatabaei, F. Evaluation of charge storage ability of chrome doped Mn_2O_3 nanostructures derived by cathodic electrodeposition. *Prog. Nat. Sci. Mater. Int.* **2016**, *26*, 523–527, doi:10.1016/j.pnsc.2016.09.006.

60. Lu, Y.; Zhang, S.; Yin, J.; Bai, C.; Zhang, J.; Li, Y.; Yang, Y.; Ge, Z.; Zhang, M.; Wei, L.; et al. Mesoporous activated carbon materials with ultrahigh mesopore volume and effective specific surface area for high performance supercapacitors. *Carbon N. Y.* **2017**, *124*, 64–71, doi:10.1016/j.carbon.2017.08.044.

61. Chen, H.; Guo, Y.C.; Wang, F.; Wang, G.; Qi, P.R.; Guo, X.H.; Dai, B.; Yu, F. An activated carbon derived from tobacco waste for use as a supercapacitor electrode material. *Xinxing Tan Cailiao/New Carbon Mater.* **2017**, *32*, 592–599, doi:10.1016/S1872-5805(17)60140-9.

62. Xi, Y.; Liu, X.; Xiong, W.; Wang, H.; Ji, X.; Kong, F.; Yang, G.; Xu, J. Converting amorphous kraft lignin to hollow carbon shell frameworks as electrode materials for lithium-ion batteries and supercapacitors. *Ind. Crops Prod.* **2021**, *174*, 114184, doi:10.1016/j.indcrop.2021.114184.

63. Qu, J.; Geng, C.; Lv, S.; Shao, G.; Ma, S.; Wu, M. Nitrogen, oxygen and phosphorus decorated porous carbons derived from shrimp shells for supercapacitors. *Electrochim. Acta* **2015**, *176*, 982–988, doi:10.1016/j.electacta.2015.07.094.